Progress In Electromagnetics Research B, Vol. 80, 37–57, 2018

A Hermite-Interpolation Discretization and a Uniform Path Deformation for the Spatial Spectral Domain Integral Equation Method in Multilayered Media for TE Polarization

Roeland J. Dilz* **and Martijn C. van Beurden**

Abstract—Two alternative approaches to the spatial spectral integral equation method are proposed. The first enhancement comprises a Hermite interpolation as the set of basis functions instead of the Gabor frame. The continuity, differentiability, equidistant spacing, and small support of these basis functions allows for an efficient and accurate numerical implementation. The second approach encompasses a method to transform between spatial domain and the deformed path in the complex-plane spectral domain. This method allows for more general path shapes, removing the need to decompose the complex-plane spectral domain path into distinct straight sections. Both enhancements are implemented for the case of TE polarization, and the results are validated against the finite element method and rigorous coupled-wave analysis.

1. INTRODUCTION

A spatial spectral domain integral equation method was introduced in [1] to compute the scattering from finite dielectric objects in layered dielectric media for transverse electric (TE) polarization. This time-harmonic method computes the interaction between the electric field and the dielectric object in the spatial domain and employs the spectral domain to compute the Green-function multiplication. By employing a rapid way of Fourier transformation between the spatial and spectral domain, an algorithm that scales as $O(N \log N)$, with N the number of unknowns is yielded. Generalizations of this method to transverse magnetic (TM) [2] polarization and full-wave 3D [3, 4] scattering in layered media have also been developed.

The translation symmetry that is present in the direction(s) transverse to the stacking direction of the layered background medium is a key to the efficacy of the spatial spectral method. In the spatial spectral method, this symmetry is exploited by transforming the transverse direction(s) to the spectral domain, where the Green tensor integral becomes a pointwise multiplication.

The conjugate gradient fast Fourier transform (CGFFT) [5, 6], method is related to the spatial spectral method, since it also computes the field material interaction in the spatial domain and employs FFTs to speed up the Green function integral. With CGFFT the it is possible to speed up the Green tensor integral up by exploiting a discrete translation symmetry in the basis functions. This discrete translation is inherited from the continuous translation symmetry in the background medium combined with a set equidistant basis functions. Using this set of basis functions the Green function integral is turned into a discrete convolution that is evaluated efficiently using FFTs and zero-padding.

Opposed to CGFFT, the spatial spectral method employs a discretization directly in the spectral domain. Therefore, the translation symmetry in the background medium can be employed fully as a continuous translation symmetry instead of a discrete translation symmetry as it is used in CGFFT.

Received 21 November 2017, Accepted 1 March 2018, Scheduled 12 March 2018
* Corresponding author: Roeland J. Dilz (r.dilz@tue.nl).
The authors are with the Eindhoven University of Technology, P. O. box 513, 5600MB Eindhoven, The Netherlands.

Therefore, the spatial spectral method can employ a Fourier transform without an equivalent of zero-padding. Throughout [1–3] the Gabor frame was employed to discretize the integral equation, which leads to an efficient means of Fourier transformation. The Gabor frame was chosen because it allows for an exact and almost trivial $O(N)$ Fourier transformation operation. However, the operation of multiplication requires a large number of small zero-padded FFTs, although it scales as $O(N \log N)$ [7]. Since the multiplication operation is relatively slow, a slightly different discretization was proposed in [4]. This approach employs FFTs for the Fourier transformation and fast $O(N)$ multiplications. An important downside of the Gabor frame is that the basis functions are not very well localized, which makes it computationally expensive to evaluate function values at a single point in the spatial or the spectral domain, since a large number of basisfunctions contribute to each point in the spatial or spectral domain. This is disadvantageous for initialization, error-control, and some of the post-processing steps.

For an efficient discretization, four demands are stated in this paper that a discretization scheme should satisfy in order to be successful for the spatial spectral integral equation method. Based on these, we introduce the Hermite interpolation as an alternative discretization scheme. One important advantage of the basis functions connected to Hermite interpolation is that they are equidistantly spaced, allowing for a Fourier transformation based on FFTs. The Fourier transform is exact on a set of equidistantly spaced points only and it is interpolated by a Hermite interpolation. Therefore, two distinct Hermite interpolations are needed, one for the spatial and one for the spectral domain. The operation of Fourier transformation is then an approximation in $\mathcal{L}^2$ sense. Additionally, the basis functions are very well localized, which allows for both fast multiplication operations and fast pointwise evaluation. Also the multiplication operation is an approximation in $\mathcal{L}^2$ sense. When the order of the Hermite interpolation moderately low, in the range $\{2, \ldots, 5\}$, it is an accurate and computationally efficient discretization.

The Green function contains poles and branch cuts on the real axis of the spectral domain [8, Chapter 8, 9, Chapter 5, 10, Chapter 4, 11, Chapter 2], which are hard to discretize. Therefore, another challenging part of the implementation of the spatial spectral integral equation method is the representation of the contrast current density, the electric field and the Green function on a path defined into the complex plane of the spectral domain. Such paths are also used to evaluate Sommerfeld integrals [12] to compute the real-space Green function in a layered medium and a large variety of different paths have been chosen already, such as the steepest descent path (SDP) [8, 13], a path that is completely different from a line over the real axis. Alternative paths that remain closer to the real spectral axis can also be employed [14, 15]. Since not only the Green function is represented on the spectral path, but also the contrast current density and the electric field, not all complex path are suitable. In [1], a path is proposed that is close enough to the real spectral axis to accurately represent the contrast current density and the electric field, while evading the problematic parts in the Green tensor. The main downside of this path is that the spectral domain is divided in three distinct regions per dimension, with different discretization methods and an elaborate scheme to transform to and from the path and a careful handling of the functions that need to be discretized. Here, we consider a different transformation method between the spatial domain and the complex-path representation in the spectral domain. These transformation methods allow for a single discretization on the spectral path, which simplifies the discretization of the Green function, requires less memory and is more flexible.

The paper starts with a brief recollection of the TE-polarized domain integral formulation. The first main subject of this paper is the Hermite interpolation as a discretization. This is introduced in Section 3, including schemes to compute the Fourier transform and some numerical examples. The second main subject of this paper concerns an alternative approach to transforming from spatial domain to the complex-plane spectral-domain path and back again. In Section 4, a representation for transformation between the spatial domain and paths through the complex plane of the spectral domain are introduced. Subsequently, this representation is used to introduce two new transformations that are applicable to a more general type of complex paths. The proposed algorithm is subsequently demonstrated on three numerical examples, where we compare the obtained results against results obtained with the finite element method (FEM) [16, 17] or rigorous coupled-wave analysis (RCWA) [18–20].

2. FORMULATION

We present an algorithm for the two-dimensional scattering problem in a layered medium as illustrated in Figure 1. The multilayered medium consists of $N-1$ layers, where layer n extends from z_n to z_{n+1}, with thickness $d_n = z_{n+1} - z_n$ and relative permittivity $\varepsilon_{rb,n}$. The upper and lower half-spaces have relative permittivities 1 and $\varepsilon_{rb,N}$, respectively. In layer i a dielectric object of finite size is located. This object is completely contained in the simulation domain $\mathcal{D} = [-W, W] \times [z_{\min}, z_{\max}]$.

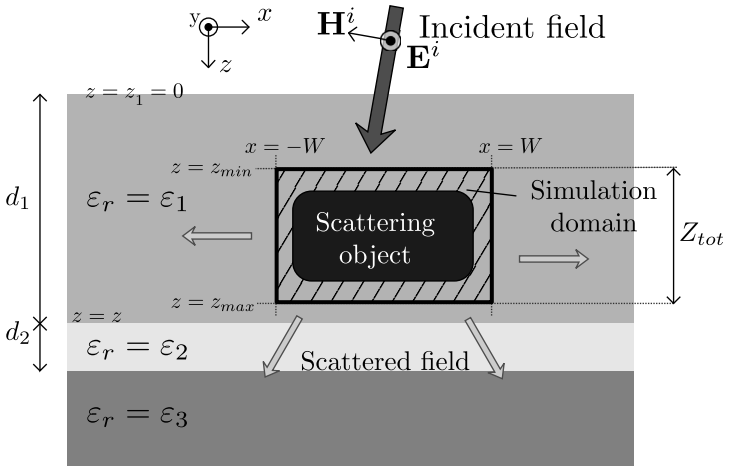

Figure 1. The two-dimensional EM-scattering problem with TE polarization for a case with two layers ($N = 3$).

The scattering of electromagnetic waves in a stratified dielectric medium by dielectric objects can be described via the electric-field integral equation (EFIE). For simplicity we briefly repeat the formulation for TE polarization in two dimensions as described in [1, 2]. This EFIE is governed by the following set of equations

$$E^s(x,z) = \int_{\mathcal{D}} dx'dz' G(x,z|x',z') J(x',z') \tag{1}$$

$$J(x,z) = \chi(x,z)\left(E^i(x,z) + E^s(x,z)\right). \tag{2}$$

Here $\mathcal{D}$ denotes the simulation domain, i.e., the domain on which the scattered electric field is to be computed. The scattered electric field $E^s(x,z)$ signifies the unknown to be computed. The incident electric field is denoted $E^i(x,z)$, e.g., a plane wave at an arbitrary angle. The contrast current density $J(x,z)$ is induced on the scattering object by E^i and E^s and is the source for the scattered field. The Green function $G(x,z|x',z')$ denotes the electric field at (x,z) generated by a point-like current source located at (x',z'). The reflections from the multilayered medium are included in the Green function. The contrast function $\chi(x,z)$ describes the scattering dielectric object as

$$\chi(x,z) = \frac{\varepsilon_r(x,z)}{\varepsilon_{rb}(z)} - 1, \tag{3}$$

where $\varepsilon_r(x,z)$ denotes the relative permittivity at position (x,z), and $\varepsilon_{rb}(z)$ denotes the relative permittivity of layered background medium, which is translation invariant in the x direction. Note that the contrast function is nonzero only on the scattering object.

3. HERMITE INTERPOLATION AS BASIS IN THE TRANSVERSE DIRECTION

3.1. General Considerations about the Discretization

In the transverse direction there is a translation symmetry in the layered background medium. This implies that the Green function is a function of $(x - x')$, instead of being a function of both x and x'

individually. This can be exploited by transforming the x coordinate in Eq. (1) to the spectral domain, with spectral variable k_x

$$E^s(k_x, z) = \int_{z_{min}}^{z_{max}} dz' G(k_x, z|z') J(k_x, z'). \tag{4}$$

An inverse Fourier transformation of $E^s(k_x, z)$ to $E^s(x, z)$ and a Fourier transformation from $J(x, z)$ to $J(k_x, z)$ are applied to evaluate the field material interaction in Eq. (2). For the Fourier transform of function $\varphi(x)$ we use the definition

$$\varphi(k_x) = \mathcal{F}_x[\varphi(x)](k_x) = \int_{-\infty}^{\infty} dx \varphi(x) e^{-jk_x x}. \tag{5}$$

Throughout the rest of this article we will omit writing down explicitly the difference between a function in the spatial domain and its Fourier transform. All functions in the spatial domain will have x as one of the arguments, and their Fourier transform will have k_x as one of the arguments.

The discretization in the transverse direction is vital for the efficiency of the algorithms developed in [1, 3, 4, 7], since both the accuracy and the computational complexity strongly depend on it. Several properties can be identified that a discretization should exhibit to allow for an accurate and efficient numerical method.

(i) The number of required basis functions should be small.

(ii) An accurate means of Fourier transformation should be available.

(iii) A rapid means of Fourier transformation should be available.

(iv) Fast addition and multiplication operators should be available for the discretized equation.

The analytical Gabor-frame discretization satisfies point 1 for large scatterers, although the broad window functions make it less efficient for small scatterers. Since the Gabor frame is a simultaneous discretization of the spatial and spectral domains, the second and third points are very well satisfied. The most important downside is that it is hampered by a slow multiplication operator in point 4.

The list-based representation of [4] improves the multiplication time at the cost of a slightly slower Fourier transformation. This considerably reduces the computational complexity, with negligible approximations made.

Although there is a significant difference in computation time, both the aforementioned discretizations are closely related in terms of discretization via a Gabor frame. Entirely different discretizations are also possible. A discrete translation invariance in the basis functions is advantageous, since that often allows the use of FFTs in the numerical implementation. Throughout the rest of this section we will consider a Hermite interpolation with equidistant basis functions and argue that it also satisfies the four points mentioned above.

3.2. Hermite Interpolation

The Hermite interpolation [21, Section 2.11] interpolates a function where the function values and (a number of its) derivatives are known. In this section we assume that the function is sampled on an equidistant Δ_x lattice and that at each of the lattice points the function value and $R-1$ derivatives are known, such that a function is represented by coefficients f_{nr} given by

$$f_{nr} = f^{(r)}(n\Delta_x), \tag{6}$$

with $n \in \{-N_x, \ldots, N_x\}$ and derivatives $r \in \{0, \ldots, R-1\}$. We will call R the degree of the Hermite interpolation. To produce the interpolation between two sample points, e.g., $x = 0$ and $x = \Delta_x$, scaled polynomials $h_{rj}(x)$ are used on this interval, which are defined as

$$h_{rj}(x) = \sum_{\ell=0}^{2R-2} \eta_{rj,\ell} x^\ell, \tag{7}$$

with indices $r \in \{0, \ldots, R-1\}$ and $j \in \{0, 1\}$. The coefficients $\eta_{rj,\ell}$ are chosen such that $h_{rj}^{(q)}(i) = \delta_{rq}\delta_{ij}$, with $q, r \in \{0, \ldots, R-1\}$ and $i, j \in \{0, 1\}$. In Figure 2, several examples are shown for these $h_{rj}(x)$

functions. From these $h_{rj}(x)$ polynomials, the basis functions for the interpolation $b_{nr}(x)$ can be obtained as

$$b_{nr}(x) = \begin{cases} 0 & \text{if} \quad x < (n-1)\Delta_x \\ \Delta_x^r h_{r1}(x/\Delta_x - n - 1) & \text{if} \quad (n-1)\Delta_x \leq x < (n)\Delta_x \\ \Delta_x^r h_{r0}(x/\Delta_x - n) & \text{if} \quad n\Delta_x \leq x < (n+1)\Delta_x \\ 0 & \text{if} \quad x > (n+1)\Delta_x, \end{cases} \tag{8}$$

Here $n \in \{-N_x, \ldots, N_x\}$ and $r \in \{0, \ldots, R-1\}$. In Figure 3 some example basis functions are shown. Now the interpolation with the coefficients from Eq. (6) is given by

$$f(x) \approx \sum_{n=-N_x}^{N_x} \sum_{r=0}^{R-1} f_{nr} b_{nr}(x). \tag{9}$$

The inner sum is nonzero only for $n = \text{floor}(x/\Delta_x)$ and $n = \text{ceiling}(x/\Delta_x)$, yielding a total of $2R$ nonzero terms in the double summation.

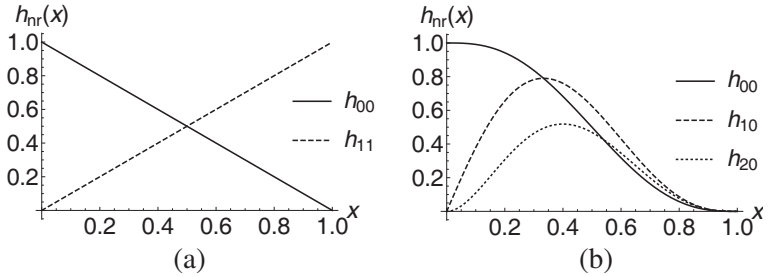

Figure 2. (a) The $h_{rj}(x)$ function for order $R = 1$. (b) Scaled $h_{0j}(x)$ function for order $R = 3$.

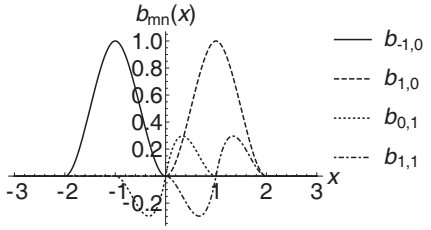

Figure 3. Hermite-interpolation basis functions for $\Delta_x = 1$ and $R = 2$.

The addition of two functions $a(x) = b(x) + c(x)$ is trivially represented by $a_{nr} = b_{nr} + c_{nr}$. The multiplication of functions, $a(x) = b(x)c(x)$, is represented by coefficients, computed from the generalized Leibnitz rule

$$a_{nr} = \sum_{\ell=0}^{r} \frac{r!}{(r-\ell)!\ell!} b_{n,(r-\ell)} c_{n\ell}. \tag{10}$$

The computation of all coefficients a_{nr} requires $O(R^2 N_x)$ operations. Therefore, we conclude that the fourth point on the list in Section 3.1 is satisfied by the Hermite interpolation as long as R is restricted to a small integer, i.e., $R \in \{2, \ldots 5\}$.

3.3. Fourier Transformation

In the spectral domain, we use Hermite interpolation as well. The Fourier transform of the approximated function in Eq. (9) is calculated analytically. The uniform sampling in the spatial domain is exploited in this Fourier transformation by employing FFTs. These FFTs dictate that (derivatives of) the analytic Fourier transformation are evaluated at an equidistant lattice in the spectral domain with

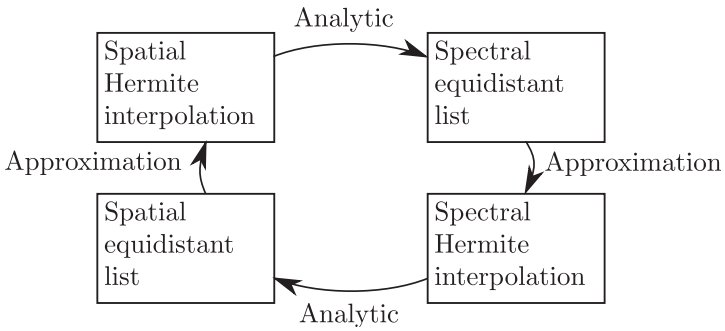

Figure 4. An analytic algorithm exist to compute function values and corresponding $R-1$ derivatives of a function on an equidistant lattice. These values are then used in a second Hermite interpolation, from which approximation errors results.

lattice constant $\Delta_k = 2\pi/(2N_x+1)$. From the analytically transformed values on this lattice in the spectral domain, a new Hermite interpolation can be devised in the spectral domain. Therefore, the analytic Fourier transform is only evaluated at an equidistant lattice in the spectral domain, and in between a Hermite-interpolated is used. Therefore, some approximation error is made. This is illustrated in Figure 4.

In the spectral domain, the Hermite interpolation is computed at N_x lattice points. The equidistant sampling in the representation of Eq. (6) and Eq. (9) allows to compute the Fourier transform as

$$f(k_x) \approx \int_{-\infty}^{\infty} dx \sum_{n=-N_x}^{N_x} \sum_{r=0}^{R-1} f_{nr} b_{nr}(x) e^{-jk_x x}, \tag{11}$$

By using Hermite interpolation in the spectral domain as well, with sampling distance $\Delta_k = 2\pi/((2N_x+1)\Delta_x)$, the coefficients in the spectral domain, f_{st} via Eq. (6), can be computed efficiently as

$$\begin{aligned} f_{st} &= f^{(t)}(s\Delta_k) = \int_{-\infty}^{\infty} \sum_{n=-N_x}^{N_x} \sum_{r=0}^{R-1} f_{nr} b_{nr}(x)(-jx)^t e^{-js\Delta_k x} \\ &= \sum_{n=-N_x}^{N_x} \sum_{r=0}^{R-1} [(-jn\Delta_x)^t f_{nr}] e^{-2\pi j\, sn/N_x} \int_{-\infty}^{\infty} (jx)^t e^{-js\Delta_k x} b_{0r}(x). \end{aligned} \tag{12}$$

Here we recognize a discrete Fourier transformation in the sum over n, which can be calculated rapidly with the FFT algorithm. The integrals can be calculated during initialization, which yields a discrete Fourier transformation from n to s for each r and t value. Therefore, the computational efficiency of the Fourier transform scales as $O(R^2 N_x \log N_x)$. Since the number of derivatives should be kept rather small, $R \in \{2,\ldots,5\}$ and N_x large, this algorithm scales well to large numbers of unknowns. We conclude that also the third point on the list in Section 3.1 is satisfied by the Hermite interpolation.

3.4. Tests of the Hermite Interpolation

Showing that the Hermite interpolation satisfies the third and fourth points on the list in Section 3.1 leaves the first two points. We now provide numerical evidence that the first two points are also satisfied.

We test the Hermite interpolation on a continuous function consisting of the sum of three modulated Gaussians, which is shown in Figure 5(a). In Figure 5(b) we show the function approximated by a Hermite interpolation of very low order $R=1$. In Figure 5(c) the $\mathcal{L}^2[-3,3]$ error is shown on a double-logarithmic scale for functions that are Hermite interpolated. Note that on the x-axis the sample spacing, Δ_x/R is shown. The lines show the trend for dense sampling (small Δ_x). Polynomial convergence is observed with a convergence of order $2R$ as indicated by the lines. For a relative error of 10^{-3}, the $R=1$ sampling requires more than 10 times more samples than the sampling with $R=5$. For comparison, the relative error for a Gabor frame is shown in Figure 5(d). It can be concluded that both Hermite interpolation and Gabor frame perform well, although the Hermite interpolation is not as efficient as

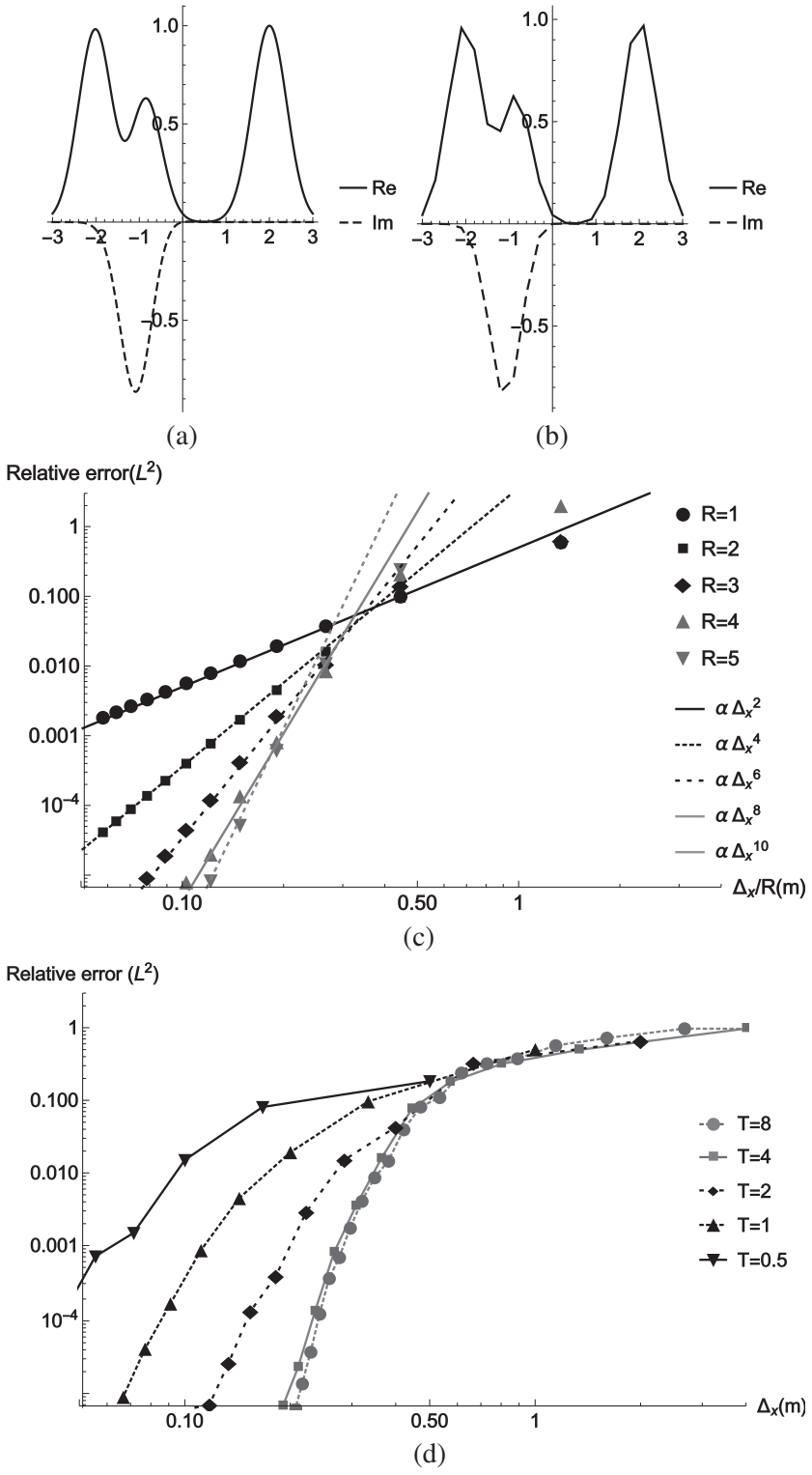

Figure 5. (a) Function used for testing, given by $\exp(-\pi(x+2)^2) + \exp(-\pi(x-2)^2) + \exp(-\pi(x+1)^2 + jx)$. (b) Function approximated with $\Delta_x = 0.3$ and $R = 1$. (c) Relative $\mathcal{L}^2$ error of approximation with Hermite interpolation for various R and Δ_x values. (d) Relative $\mathcal{L}^2$ error of approximation with a Gabor frame. Here $\Delta_x = \alpha X/(2N+1)$, with N the range of the n-sum in Eq. (16) of [7], which is equivalent to a sample spacing of Δ_x/R in (c). An oversampling of $\alpha = \beta = \sqrt{2/3}$ for the Gabor frame was used.

the Gabor frame. Although the high-R sampling is not as efficient as the Gabor-frame discretization shown in Figure 5(d), both methods perform well. It should be noted that the large window widths, where the Gabor frame has a clear advantage, are only efficient for large simulation domains. Since the Gabor frame decays slowly to zero at the ends of the simulation domain, several extra windows are required to allow for this decay. Clearly, the Hermite interpolation is a competitive discretization and point one on the list in Section 3.1 is satisfied.

It remains to be determined how accurate the Fourier transformation associated with Hermite interpolation, Eq. (12), performs. As explained in Section 3.3 and Figure 4, the forward Fourier transformation and inverse Fourier transformation contain an approximation where a Hermite interpolation basis is used in the spectral and spatial domain, respectively. To demonstrate the impact of this approximation, a simulation domain with $N_x = 200$ and $\Delta_x = 1$ is chosen. This corresponds to $\Delta_k = 2\pi/401$ in the spectral domain. We check how a modulated Gaussian is transformed from the spatial to the spectral domain and back with Eq. (12) and its inverse, i.e., a full round in Figure 4. The Gaussian is chosen as

$$g_{X,K}(x) = \exp\left(-(x-X)^2/401 + jKx\right), \tag{13}$$

and we will use the symbol $\tilde{g}_{X,K}(x)$ to denote the back-and-forth transformed Gaussian. This function $\tilde{g}_{X,K}(x)$ approximates $g_{K,X}(x)$ best for small X and small K, since then $g_{X,K}$ exhibits the slowest oscillation in the spectral and spatial domain, respectively. A sample of $\tilde{g}_{X,K}$ and its approximation error are shown in Figure 6. As a measure of the total error in the approximation, we use the relative error based on the $\mathcal{L}^2[-X, X]$-norm. In Figure 7, we show how the approximation error depends on the position in the XK-plane. When a relative error of 10^{-3} is required, the useful domain for the Hermite upper index $R = 1$ is negligible. For larger R, the domain expands quickly, to almost the complete simulation domain for $R = 4$. Therefore, we conclude that this Fourier transformation is accurate for $R > 1$. Hence, Point 2 in Section 3.1 is also satisfied and therefore all points on the list in Section 3.1 are satisfied, when a proper value for R is chosen. Note that a small R corresponds to low accuracy and that a large R corresponds to slow Fourier transformations, so a trade-off between both is necessary. For our purpose, $R = 4$ is a proper choice. Strictly speaking, we have only shown numerical evidence for modulated Gaussian functions, which are just the type of functions used for the discretization in [1–4, 7]. Hence, any function that is important within this formulation can also be transformed on a Hermite-interpolation basis.

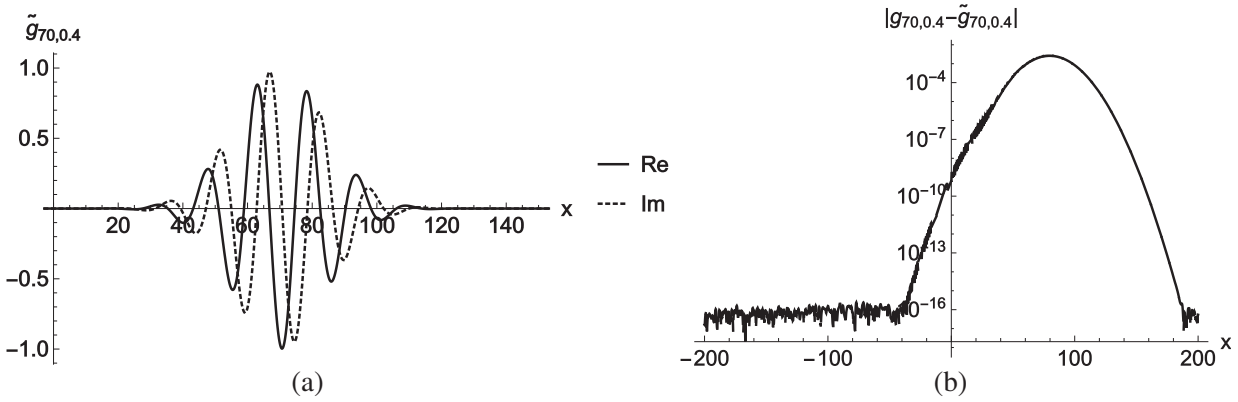

Figure 6. (a) A plot of $\tilde{g}_{70,0.4}(x)$ for $R = 2$. (b) The absolute error in $\tilde{g}_{70,0.4}(x)$, compared with the original function $g_{70,0.4}(x)$.

4. A CONTINUOUSLY DIFFERENTIABLE PATH IN THE SPECTRAL DOMAIN

4.1. Introduction

Since the multilayer Green function contains poles, branch cuts, and fast oscillations on the real k_x-axis, a small displacement into the complex plane is used to represent all quantities depending on k_x, as was

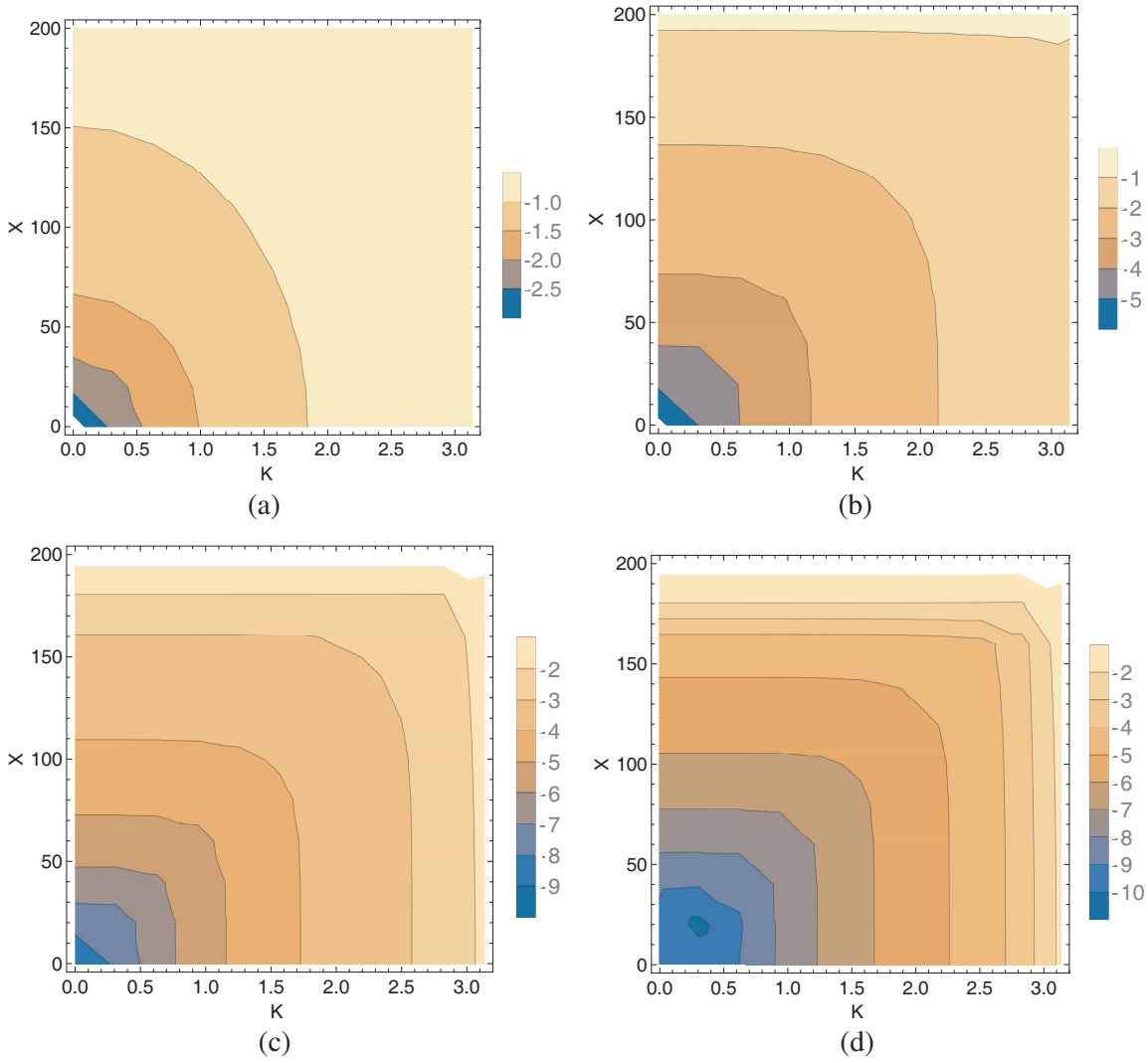

Figure 7. The $\log_{10}$ of the relative error in the approximation of the Fourier transform of the modulated Gaussian in Eq. (13) as a function of the location of its peak in the spatial and spectral domain. (a) $R = 1$, (b) $R = 2$, (c) $R = 3$, (d) $R = 4$. Notice the different scales in the legends.

described in [1]. On this complex spectral path the poles, branch cuts, and fast oscillations of the Green function are circumvented. In [1] a continuous path with a piecewise constant derivative is proposed. This path has the disadvantage that the spectral domain has to be decomposed into three pieces per transverse dimension, which is especially tedious for a three-dimensional scattering problem [3]. By choosing a path that is continuously differentiable, such a decomposition of the spectral domain is not necessary.

A significant part of the computation time involves transformations between the spatial domain and the complex path in the spectral domain. For the piecewise path in [1] an optimized method was developed that allows fast and efficient transformations between the spatial domain and the complex spectral path. Here, we present optimized methods for more general path shapes, allowing for a continuously differentiable path.

We begin by showing a more general way to represent a class of fast transformations between the spatial domain and the complex spectral path. This class of fast transformations assumes the availability of a rapid means of Fourier transformation, multiplication, and summation as indicated in Section 3.1. Subsequently we will shown how the transformations to and from the complex spectral path that was

used in [1, 3, 4, 7] can be represented in this form. Afterwards, several alternative approaches to such a transformation are proposed and discussed. Based on these alternative transformations, a continuous path in the spectral domain is proposed and tested.

4.2. Transformations to and from a Complex Spectral Path

We are interested in small path deformations $k \to \tau(k)$, with real-valued k, that can be described by $\tau(k) = k + jc(k)$. We assume $c(k)$ to be real valued and small, i.e., $|c(k)| < A$ with A on the order of Δ_k, the resolution of the discretization in the spectral domain. The transformations that interest us are the transformation of a function $f(x)$ from the spatial domain to the complex spectral path, i.e.,

$$f(\tau(k)) = \int_{-\infty}^{\infty} dx f(x) e^{-jxk} e^{c(k)x}, \tag{14}$$

and the transformation from the spectral path back to the spatial domain

$$f(x) = \int_{-\infty}^{\infty} dk (1 + jc'(k)) f(\tau(k)) e^{jxk} e^{-c(k)x}, \tag{15}$$

which is found by means of a substitution $k \to \tau(k)$ in the Fourier integral of $f(k)$. The difference between the integrals in Eqs. (14) and (15) is minor, i.e., the multiplication by the factor $(1 + jc'(k))$ does not pose a problem and then we are left with two integrals of the same form. Both integrals resemble a Fourier integral, except for the factor $\exp(\pm c(k)x)$. Since we assume that a rapid Fourier transformation is available (cf. Section 3.1), we will approximate Eqs. (14) and (15) as a sum of Fourier transformations. When we approximate

$$\begin{aligned} e^{c(k)x} &\approx \sum_{n=1}^{N} a_n(x) b_n(k) \\ e^{-c(k)x} &\approx \sum_{n=1}^{N} a_n^i(x) b_n^i(k), \end{aligned} \tag{16}$$

where the functions $a_n(x)$, $a_n^i(x)$, $b_n(k)$, and $b_n^i(k)$ remain to be defined, and the superscript ^{i} indicates the functions for the inverse transformation. Such approximations are available and valid, since $c(k)$ is bounded by A, which is on the order of the spectral resolution $\Delta_k = \pi/W_x$ and in the spatial domain functions are not evaluated outside of the simulation domain, i.e., we have $|x| < W_x$. It means that $\exp(\pm c(k)x)$ is bounded. With the path deformation as in [1], this approximation of the integral in Eq. (14) is usually chosen such that $0.05 < \exp(\pm c(k)x) < 20$ for x in the simulation domain. The transformations of a function f to and from the spectral path in Eq. (14) and Eq. (15) can then be rewritten as

$$f(\tau(k)) = \sum_{n=0}^{N} b_n(k) \int_{-\infty}^{\infty} dx a_n(x) f(x) e^{-jxk} \tag{17}$$

$$f(x) = \sum_{n=0}^{N} a_n^i(x) \int_{-\infty}^{\infty} dk (1 + jc'(k)) b_n^i(k) f(k) e^{jxk}. \tag{18}$$

These are sums of ordinary Fourier integrals. So when the functions $f(x)$ or $f(k)$ are represented by a Hermite interpolation, they can be computed efficiently, with the aid of the Fourier transformation in Eq. (12) and its inverse. The Hermite interpolation of $a(x)$, $a^i(x)$, $b(k)$ and $b^i(k)$ can be computed during initialization. Hence, these transformations consist of $(N + 1)$ FFTs, and therefore, a small N is highly important. The challenge is to find an efficient approximation in the form of Eq. (16) for a small number of terms.

4.3. The Piecewise Path

In [1] a complex spectral path was introduced given by

$$c(k) \in \begin{cases} -jA & \text{if} \quad k < -A \\ jk & \text{if} \quad -A \leq k < A \\ jA & \text{if} \quad k > A. \end{cases} \tag{19}$$

This path consists of three distinct parts with distinct discretizations, f_L, f_M, and f_R as shown in Figure 8. The Gabor frame is used as a discretization on f_L and f_R and a Taylor series on f_M. Therefore, the complex-plane representation [1] differs from the one in Section 4.2, where a single discretization is used throughout the whole path. However, the representations for f_L and f_R can be represented in the same form as Eqs. (17) and (18). We now associate the $_L$ subscript with the spectral representation on the left horizontal part of the integration path in Figure 8 and the first line in Eq. (19). We associate the $_R$ subscript with the right horizontal part in Figure 2(a) in Figure 8 and the third line in Eq. (19). This notation is applied in Eqs. (17) and (18) to yield expressions Eq. (19) given in [1] and Eq. (22) given in [1] when

$$\begin{aligned} a_L(x) &= a_R^i(x) = e^{Ax} \\ a_R(x) &= a_L^i(x) = e^{-Ax} \\ b_L(k) &= b_R(k) = 1 \\ b_L^i(k) &= b_R^i(-k) = \begin{cases} 1 & \text{if} \quad (k < A) \\ 0 & \text{if} \quad (k \geq A). \end{cases} \end{aligned} \tag{20}$$

For the middle part (M) of the path, fast methods of Fourier transforming are not applied. The transformation to the spectral domain is approximated from the fit of a Taylor series to data points and the transformation back to the spatial domain is carried out by computing the integrals in Eq. (15) directly. This method is not very optimized, but since the M-part is small, not much computation time is used. A more optimized method for this part was presented in [22].

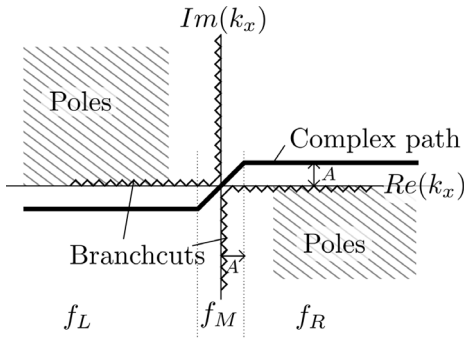

Figure 8. The complex-plane path deformation in the spectral domain as introduced in [1].

4.4. Approximation by Taylor Series

It is possible to approximate $\exp(\pm c(k)x)$ via a Taylor series as

$$\begin{aligned} e^{c(k)x} &\approx \sum_{n=0}^{N_t} c^n(k) \frac{x^n}{n!} \\ e^{-c(k)x} &\approx \sum_{n=0}^{N_t} c^n(k) \frac{(-x)^n}{n!}. \end{aligned} \tag{21}$$

Compared to Eq. (16), we can identify $a_n(x) = x^n/n!$, $a_n^i(x) = (-x)^n/n!$ and $b_n(k) = b_n^i(k) = c^n(k)$. An advantage of this method is that it allows for more general path shapes, whereas the piecewise path

in Section 4.3 uses the fact that $c(k)$ is constant over most of the domain. It is advantageous to use a smooth path deformation, since that will yield a smooth $f(\tau(k))$ and therefore splitting up the spectral domain in different parts is no longer needed. Throughout the rest of this article we will therefore use the continuously parametrized path

$$\tau(k) = k + jc(k) = k + jA\mathrm{erf}(s\sqrt{\pi/2}k/A), \tag{22}$$

where the parameter A again has the meaning of the amplitude of the deformation, and s defines the slope of $c(k)$ around 0. In Figure 9 $c(k)$ is plotted for Eq. (22).

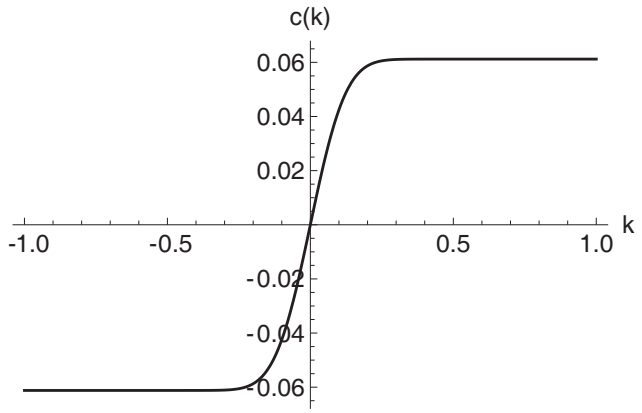

Figure 9. The imaginary part $c(k)$ of $\tau(k)$ in Eq. (22) for $s = 0.5$ and $A = 0.06$.

Next, we evaluate the accuracy of the Taylor-based version of the transformation to the spatial domain, i.e., Eq. (18), for the analytic Fourier transform of a Gaussian pulse that equals $f(k) = \mathcal{F}_x[\exp(0.1(x-10)^2)](k)$. The numerical data is based on Hermite-interpolation-based Fourier transforms with $N_x = 38$, $\Delta_x = 4/3$, $R = 4$, $\Delta_k = A = 0.612$. In Figure 10(a), the result of the transformation to the spatial domain is shown. A very low order Taylor-series approximation with $N_t = 2$ was applied, which results in a visible error. In Figure 10(b), the absolute error is shown for transforming this same Gaussian pulse with higher-order Taylor approximations. Clearly, the error is larger for large x. This was to be expected, since the truncated Taylor series in Eq. (21) loses accuracy for large x. A key point to notice is that the approximation error at a certain location, let us call it location x, does not only

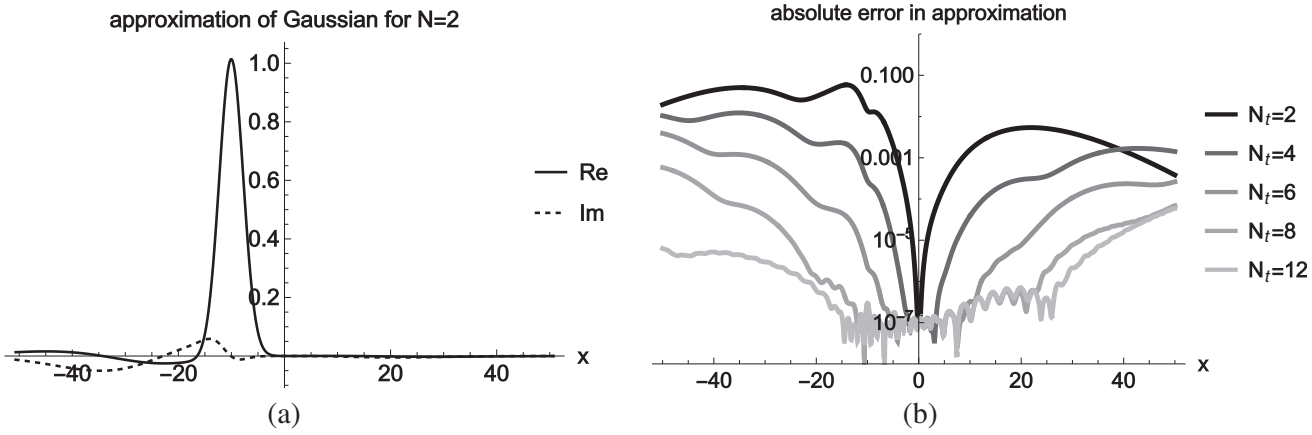

Figure 10. (a) The analytic Fourier transform of a Gaussian pulse $f(k) = \mathcal{F}_k[\exp(0.1(x-10)^2)](x)$ is sampled and then numerically transformed to the spatial domain using transformation Eq. (18) with approximation Eq. (21) for $N_t = 2$. (b) Approximation error for the same Gaussian pulse, transformed with order-N_t Taylor series approximations.

depend on the original function evaluated at x, but also on the original function at every other location x'. Therefore, the approximation error in the Fourier transformations should be considered globally, not locally in a point by point manner. For this reason we show the absolute approximation error instead of the error relative to the original function in Figure 10(b) and onward.

Instead of using the Taylor series in Eq. (21) as a power series to approximate $\exp(-c(k)x)$, we have also used a fitted power series that is more accurate for large arguments, at the cost of the accuracy for small arguments. In Figure 11(a) we see the approximation of $\exp(Ax)$, which corresponds to $\exp(-c(k)x)$ for large values of k. Clearly, the fitted approximation has a wider range of validity. This is tested by transforming the spectral representation of $\sum_{n=-3}^{3}\exp(0.1(x-10n)^2)$ to the spatial domain. The result is shown in Figure 11(b). In Figure 11(c), it is observed that the fitted approximation performs better for large x. With larger numbers of terms, the accuracy of the fit and the Taylor series improves.

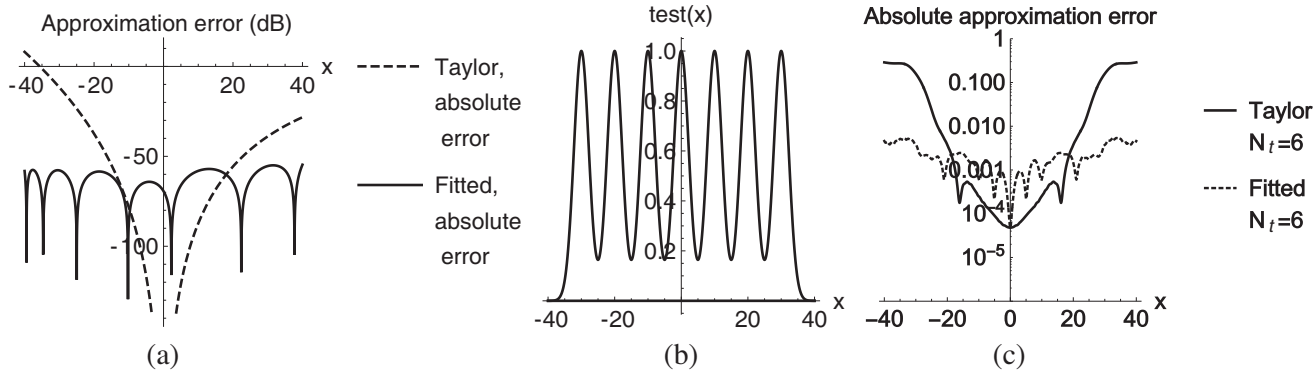

Figure 11. (a) An approximation of $\exp(Ax)$ valid for $x \in [-40, 40]$ compared to a Taylor series with the same number of terms. (b) A set of Gaussian pulses $\sum_{n=-3}^{3}\exp(0.1(x-10n)^2)$, whose representation on the spectral path is used as an input for the transformation from the path in Eq. (22) to the spatial domain. (c) The error made in the transformation to the spatial domain using Eq. (18) for a fitted polynomial and a Taylor series.

4.5. Approximation by Analytical Expansion

A second approach to transform to and from the complex spectral integration path employs an analytical continuation of the Fourier transform to a region close to the equidistant values on which the Hermite interpolation is defined. This is especially useful for calculating the transformation from the spatial to the spectral domain in Eq. (17). For the transformation of the scattered electric field back to the spatial domain, this method is less reliable since the spectral scattered electric field, Eq. (4), contains the Green function, which is not analytic close to real k_x-axis for lossless background media. Therefore, we concentrate on the transformation from the spatial to the spectral domain.

Assume that we would like to calculate $f(k^*)$ and its derivatives at $k^* \in \mathbb{C}$, while values or derivatives of f are known only at some nearby points $\{f^{(d_1)}(k_1), f^{(d_2)}(k_2), \ldots, f^{(d_{N_s})}(k_{N_s})\}$. For example, the values that are computed with the aid of the rapid Hermite-interpolation-based Fourier transformation in Eq. (12), yield values and derivatives up to order $R-1$ at an equidistant grid. From that we can select values close to k^*, from which we approximate $f(k^*)$. We expand $f(k)$ in a Taylor series t_f around k^*, i.e.,

$$t_f(k) = \sum_{n=0}^{N_f} w_n \frac{(k-k^*)^n}{n!}. \tag{23}$$

When $N_s = N_f$, the weights in the Taylor expansion can be found from solving the associated Vandermonde system

$$\text{for all } n \in 1, \ldots, N_s: \quad t_f^{(d_n)}(k_n) = f^{(d_n)}(k_n),$$

for w_n. This technique is closely related to the method in Section 5.3 in [1] and Section 4.2 in [3]. When this Vandermonde system is solved via a marix-inverse, the coefficients w_n are then simply a list of derivatives. For $N_s > N_f$ a pseudo-inverse is employed. Since this Vandermonde system is small, problems with a poorly conditioned system are easily avoided by taking $N_s > N_f$.

In the case of Hermite interpolation, this analytical continuation is especially useful, since functions are represented by an equidistant list of the function values and $R-1$ derivatives. The Hermite interpolation already uses the analyticity of the functions, since the basis functions are a local power-series expansion. This implies that an analytical expansion holds up to a distance on the order of the resolution Δ_k. Therefore, the result of a single Fourier transformation, which yields values on the real k axis, can be analytically expanded to any complex deformation, provided that the imaginary part of the path deformation is of the same order as Δ_k.

A numerical example is considered in Figure 12 for the modulated Gaussian pulse

$$g(x) = 0.1769e^{-0.1(x+15)^2+0.4jx}, \tag{24}$$

where the prefactor is chosen to normalize the peak to unit amplitude in Figure 12. We have chosen $k^* = j\Delta_k$, and the Hermite interpolation of Figure 10 is used. The Fourier transformation of Eq. (12) is applied to find a numerical approximation of $g(k)$ and the result is analytically expanded into the complex plane to $g(k + j\Delta_k)$. Figure 12(a) shows $g(k + j\Delta_k)$ and an approximation where only $g^{(0)}(0), \ldots, g^{(3)}(0)$ were used to find the approximation for $N_f = 4$. In Figure 12(b), the error is shown for this approximation with $N_f = N_s = 4$. Also two higher-order approximations are added, where $g^{(0)}(k'), \ldots, g^{(3)}(k')$ were added to the expansion with $k' \in \{-\Delta_k, 0, \Delta_k\}$ for $N_f = 8 < N_s = 12$ and $k' \in \{-2\Delta_k, -\Delta_k, 0, \Delta_k, 2\Delta_k\}$ for a total of $N_f = 12 < N_s = 20$ terms in the Taylor expansion. In Figure 12(c), it can be observed that this approximation is also successful for derivatives. The link

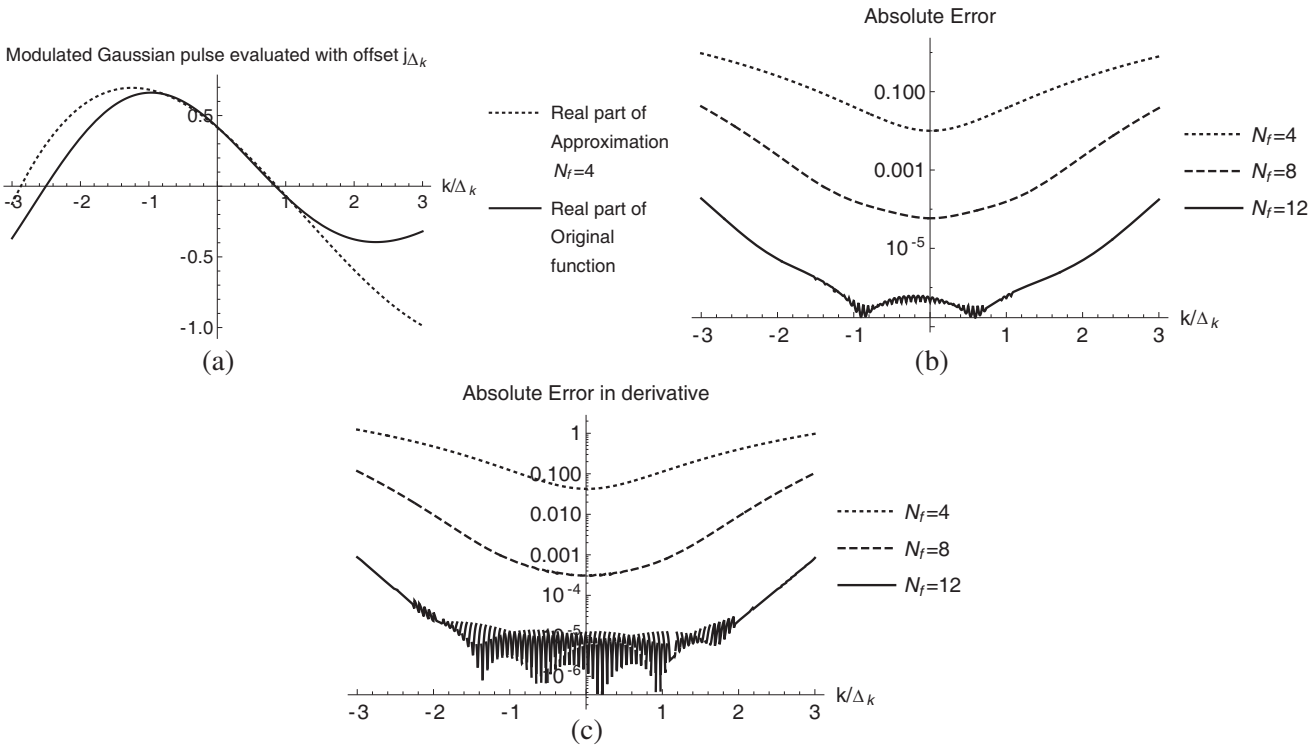

Figure 12. (a) The Fourier transformed modulated Gaussian pulse in Eq. (24) evaluated at complex coordinates, and its 4th order Taylor approximation. (b) The error for higher order approximations of Eq. (24). (c) The error in the derivative for higher order approximations of Eq. (24).

between such an analytical expansion and the function $a_n(x)$ and $b_n(x)$ in Eq. (17) is that we can choose

$$\begin{aligned} a_n(x) &= (jx)^{d_n} e^{j(k_n - k^*)x} \\ b_n(x) &= 1. \end{aligned} \tag{25}$$

5. NUMERICAL EXAMPLES

Here, we apply the methods described in Sections 3 and 4 to two selected electromagnetic scattering problems, where a plane wave is of wavelength λ is incident on a scattering object. The first testcase, Figure 13(a), consists of a single dielectric rectangle embedded in a layered medium. This testcase resembles the first testcase in [1], with only one scattering object. The second testcase consists of 32 uniformly spaced equal dielectric blocks placed on top of a lossy dielectric halfspace. This is a larger version of the third testcase considered in [1].

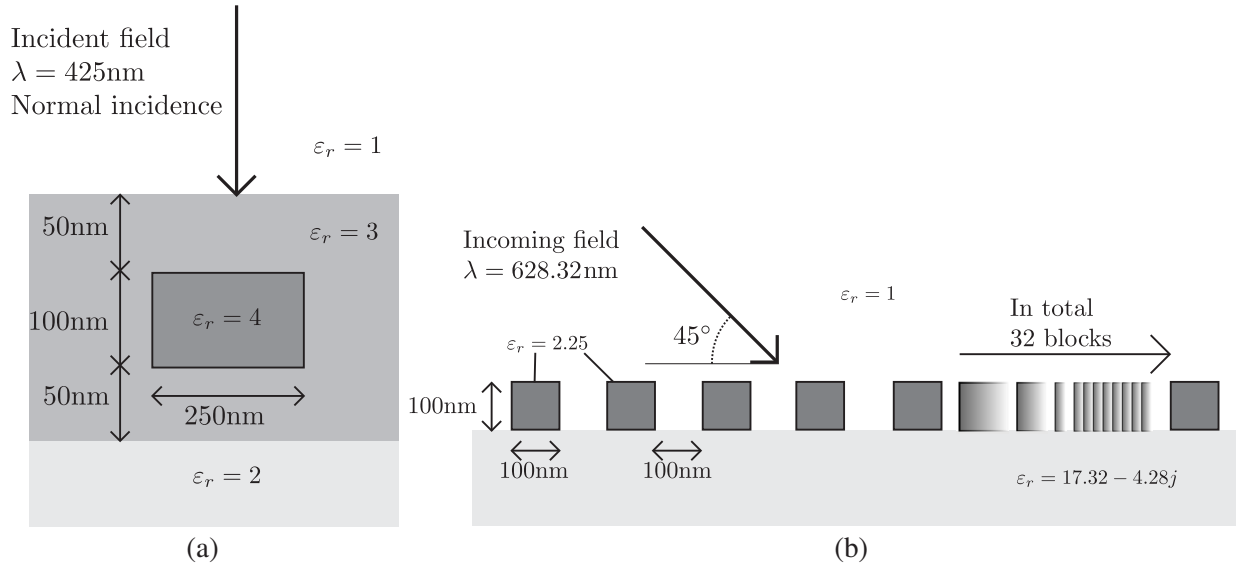

Figure 13. The two testcases that are used for validation: (a) First case: a single dielectric rectangle, embedded in a dielectric layer. (b) Second case: a grating consisting of 32 dielectric rectangles.

A Hermite interpolation was used as a discretization of order $R = 4$. The transformation to the spectral domain was carried out by applying the method in Section 4.5, where we choose $N_f = 5R$ in Eq. (23), with derivatives 0 to $R - 1$ at points $k + \{-2\Delta_k, -\Delta_k, 0, \Delta_k, 2\Delta_k\}$. For the transformation to the spatial domain the method in Section 4.4 was used with a Taylor series of N_t terms as indicated in Table 1. The value for A that determines the shape of the path in Eq. (22) was chosen $A = 3/2\Delta_k$. The rest of the simulation parameters is indicated in Table 1.

Table 1. Simulation parameters for the plots in Figures 13–19.

Variable	block	grating	chirped grating
$x_{\max}$	1200 nm	5 µm	10 µm
Δ_x	3.333 nm	10 nm	10 nm
λ	425 nm	628.32 nm	628.32 nm
Δ_z	0.104 nm	2.5 nm	2.5 nm
N_z	961	41	15
N_t	12	16	16
# Unknowns	2779212	114964	12060
Relative Error	$8.4 \cdot 10^{-7}$	$1.12 \cdot 10^{-3}$	no reference

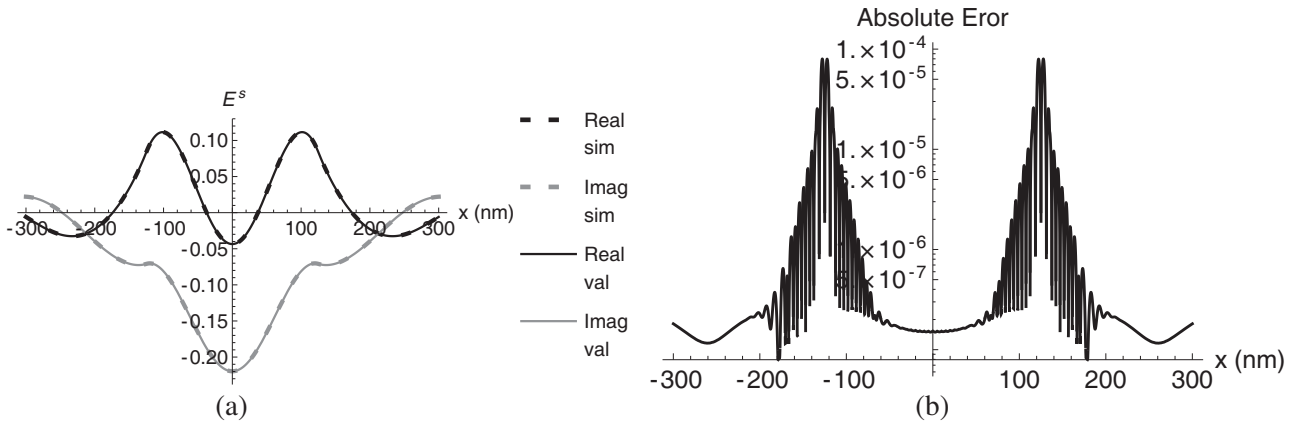

Figure 14. (a) Simulation results for the case in Figure 13(a). (b) The absolute difference between results obtained with the present algorithm and a validation using JCMWave.

For the first testcase a very fine sampling was employed to achieve a high accuracy. In Figure 14(a), the electric field is shown along the horizontal line exactly through the middle of the scattering object. The validation result is computed using the commercial software JCMWave [17]. The absolute difference between results obtained with the algorithm in this paper and JCMWave are shown in Figure 14(b). Clearly there are two peaks in the absolute error, corresponding to the edges of the block. We employed a smoothened contrast function $\tilde{\chi}(\mathbf{x})$ calculated via

$$\tilde{\chi}(k_x, z) = \frac{1}{4}\chi(k_x, z)\mathrm{erfc}(1.67k_x - 0.42N_x\Delta_k)\mathrm{erfc}(-1.67k_x + 0.42N_x\Delta_k) \tag{26}$$

from the exact contrast function (3). This smoothening leads to localized Gibbs-phenomenon-like oscillations of the contrast function. These oscillations are the cause of the error originating from the edges of the scattering object.

Around the center of the object, on the interval $x \in [-70, 70]\,\mathrm{nm}$, where the Gibbs-phenomenon does not dominate the error, we have computed the $\mathcal{L}^2$ relative error to be $8.4 \cdot 10^{-7}$. Using this method to measure the accuracy of the presented method, we show how the simulation error converges in Figure 15 for the most important simulation parameters, x_{max}, R, Δ_x and Δ_z. For each figure we kept all simulation parameters equal to the ones displayed in Table 1, except for the one in which the convergence is studied. It should be noted that the convergence for large $x_{\max}$ stalls in Figure 15(a) since the accuracy there is limited by the other simulation parameters, most notable Δ_z. This parameter is important since it determines Δ_k. In Figure 15(b) the convergence with respect to the order R is shown. The increased error resulting from a low order R can be explained by the increased error in the Fourier transform as shown in Figure 7. Increasing $x_{\max}$ can mittigate the effects of lowering the order R, since it increases the complete simulation domain and therefore it also increases the the size of the simulation domain where the Fourier transform can be computed accurately. From Figure 15(c) we can conclude that the error decreases when Δ_x is lower and the discretization becomes finer. Similarly, in Figure 15(d) we see that the error also decreases when Δ_z is lower and the discretization becomes finer.

The scaling of the computation time of the algorithm with the described discretization in the x-direction is plotted in Figure 16. In Figure 16(a) the timing is shown against $x_{\max}$, which is directly proportional to the number of sample point in the x-direction and a linear scaling is observed, where an $O(x_{\max} \log x_{\max})$ would be expected because of the use of FFTs. However, at these simulation settings, the time required for other operations still dominates over the time required for the FFTs. In Figure 16(b) the timing is shown against the order R of the Hermite interpolation and a quadratic scaling is observed, as was to be expected from Eqs. (12) and (10). Note that the timings were taken at $\Delta_z = 2.5\,\mathrm{nm}$ instead of the value in Table 1, which yields a relative accuracy of $0.94 \cdot 10^{-3}$ for $R = 4$ and $x_{\max} \geq 60\,\mathrm{nm}$. It should be noted that timings were taken with a non-optimitized implemation built with the Mathematica software package.

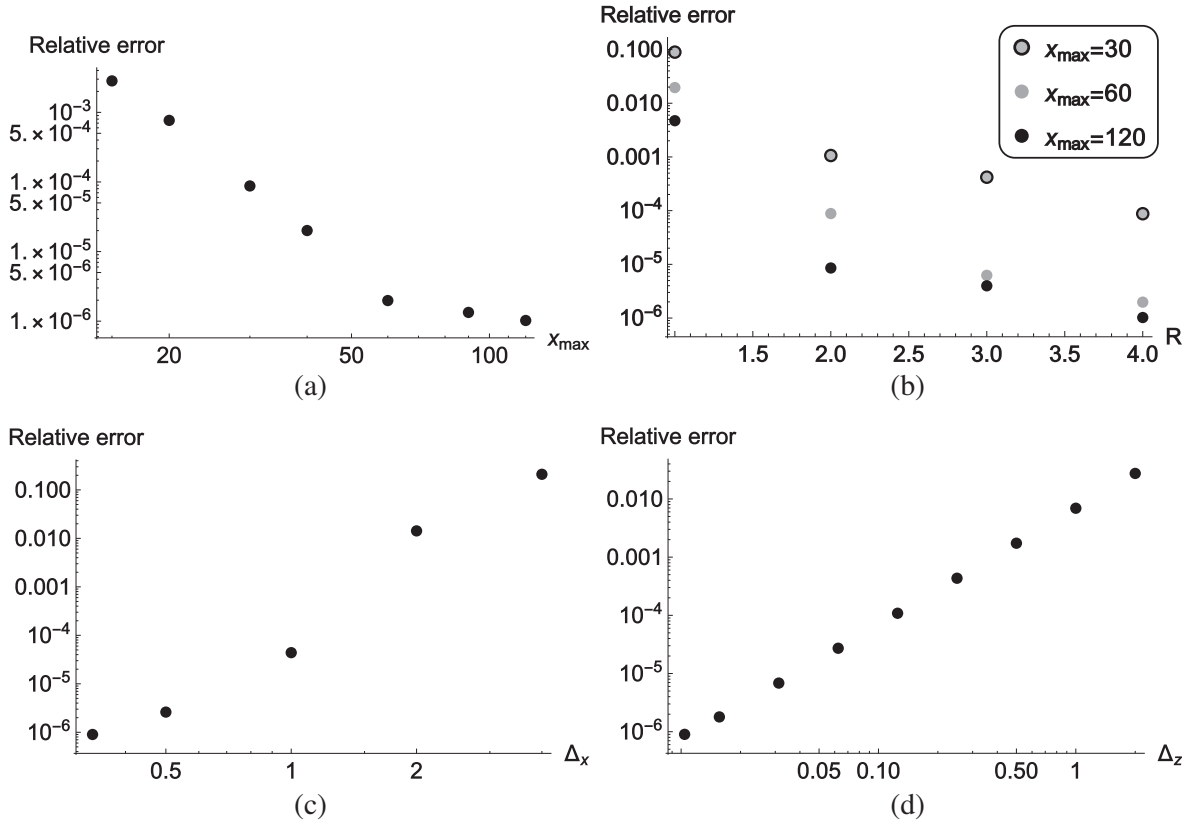

Figure 15. The convergence of the $\mathcal{L}^2$ relative error of the scattered field for x in the interval $[-70, 70]$ nm. All simulation parameters were chosen as in Table 1, with the exception to the parameter against which the convergence is shown. In (a) the convergence is shown against the size of the simulation domain, $x_{\max}$, in (b) against the Hermite interpolation order R and different values of $x_{\max}$, in (c) against the sample rate of the Hermite interpolation Δ_x, and in (d) against the sample rate in the vertical direction Δ_z.

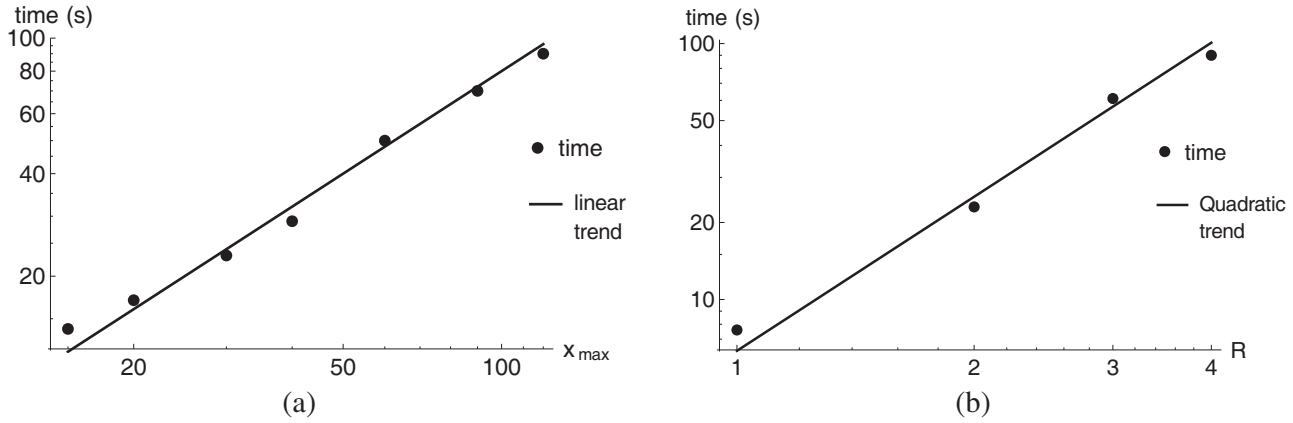

Figure 16. The computation time as a function of two parameters that govern the accuracy in the x-direction, i.e., $x_{\max}$ in (a) and R in (b). Note that these computations were carried out with a lower $\Delta_z = 2.5$ nm than in Table 1. The relative accuracy at the highest computation time was $0.94 \cdot 10^{-3}$ for both (a) and (b).

For the second testcase we have used the simulation parameters as displayed in Table 1. The scattered electric field E^s is plotted in Figure 17(a) at the horizontal line at the top of the dielectric substrate. We have validated our results against an implementation of RCWA with perfectly matched layers absorbing boundaries [20] with a total of 320 harmonics included. An $\mathcal{L}^2$ relative error level of $1.12 \cdot 10^{-3}$ was observed over the domain containing the blocks. This accuracy was reached with the simulation parameters as listed in Table 1. Notice that the number of unknowns was chosen much smaller than for testcase 1, although the simulation domain was much larger, hence the somewhat larger discrepancy between our results and the RCWA validation data. In Figure 17(b), the absolute difference between the data obtained with the present algorithm, compared to the RCWA results for various values of $x_{\max}$. The effect of a small $x_{\max}$ is clearly visible as a large simulation error at large x. This large error is due to the error originating from the transformations between the spatial and spectral domain, since the accuracy deteriorates quickly towards the edges of the simulation domain at $x_{\max}$ as depicted in Figure 7. However, good simulation results are obtained for a simulation domain of $2x_{\max} = 10\,\mu\text{m}$, which shows that zero padding to twice the simulation size ($2 \times 6.4 = 12.8\,\mu\text{m}$) is not required, as opposed to, e.g., CGFFT.

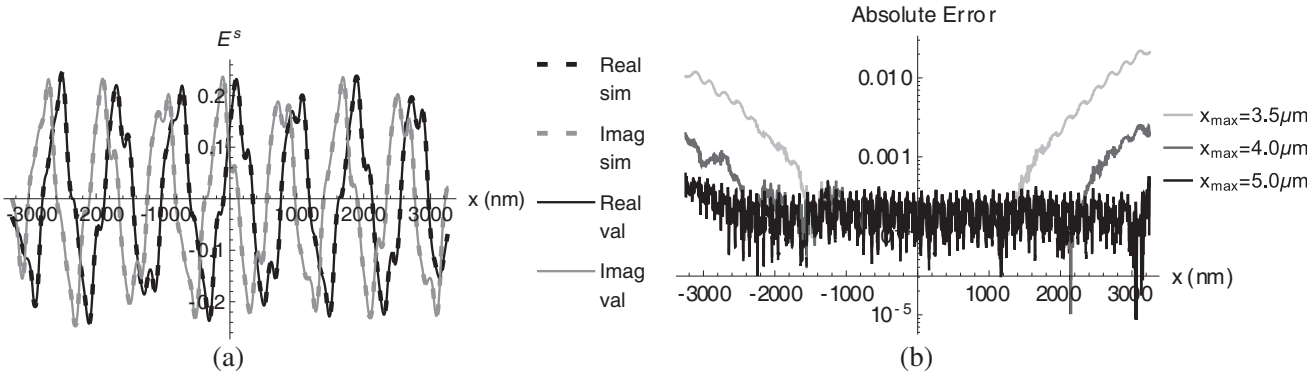

Figure 17. (a) Simulation results for the case in Figure 13(b). (b) The absolute difference between results obtained with the present algorithm and a validation using RCWA.

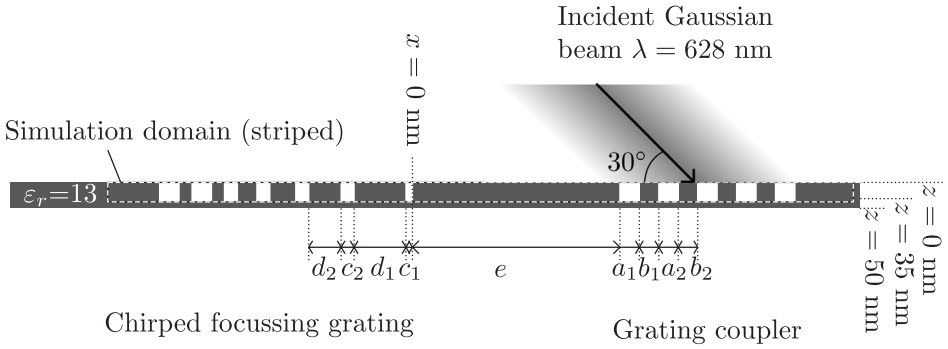

Figure 18. A gratingcoupler (right) couples an incoming Gaussian wave towards a chirped grating (left) emits a focussed beam.

The final testcase is designed to show that the algorithm can be used for more complicated structures as well than the previous testcases. The layered medium consists of a single layer of high ($\varepsilon_r = 13$) contrast, that supports a single guided wave. On the right wave a focused Gaussian beams is input on a grating coupler, inspired by [23]. This inserts a guided wave into the dielectric layer that travels to the left. On the left a chirped grating is located that emits a beam focused around four wavelengths above the structure, inspired by [24, 25]. The dimensions of both the gratingcoupler and the focussing chirped grating, as described in Table 2, have not been thoroughly optimized for the best response, since this

Table 2. Dimensions the third testcase in Figure 18.

Parameter	size
a_i	56 nm for $i \in \{1, \ldots, 10\}$
b_i	250 nm for $i \in \{1, \ldots, 10\}$
c_i	$\{84, 88, 92, 96, 100, 104, 108, 112, 116, 120, 124, 128,$ $132, 136, 140, 144, 148, 152, 156, 160, 164, 168, 172\}$ nm
d_i	$\{342, 330, 314, 297, 279, 258, 238, 215, 195, 174, 156, 139, 124, 110,$ $99, 87, 79, 70, 62, 54, 48, 42\}$ nm
e	4.40 µm

is outside the scope of this article. The incoming Gaussian beam of unit amplitude is described by

$$E^i(x,z) = A\int_{-k_0}^{k_0} dk_x e^{-w\left(\frac{k_x - k_0\sin(\theta)}{k_0}\right)^2 + jk_x x_0} e^{jk_x x + jk_z z}, \tag{27}$$

where we choose A to normalize the incident field to unit amplitude at its maximum on $z = 0$. The rest of the constants were chosen $w = 40$, $\theta = 30°$, $x_0 = 400$ nm.

In Figure 19(a) we show the of the real part of the electric field. On the right we see the incoming wave and its reflection from the surface of the layer. A guided wave is coupled into the layer, propagating energy to the left. Part of this energy is focused up- and downwards by the chirped grating towards a foci at about 2.5 µm from the layer. Another part of the energy in the guided wave continues on traveling to the left in the gratingcoupler. In Figure 19(b) we show the logarithm of the field strength. A strong standing-wave behaviour is observed between the coupler and the chirped grating.

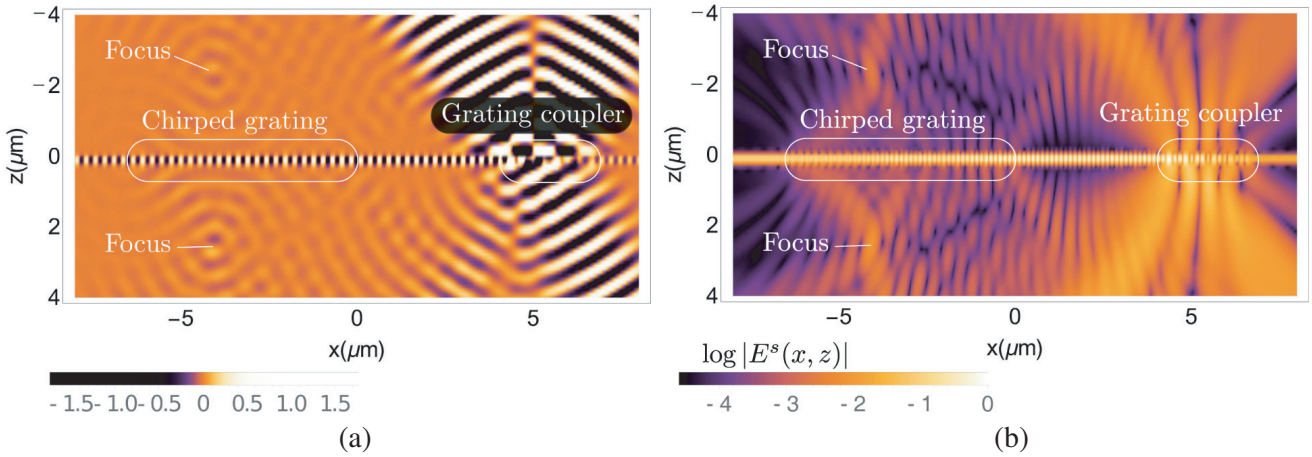

Figure 19. (a) The real part of the electric field. (b) A logarithmic plot of the scattered electric field E^s.

6. CONCLUSION

We introduced a Hermite interpolation as basis functions for the spatial spectral method for a domain integral equation for 2D TE scattering in a dielectric layered medium. The continuous nature of the basis functions allows for accurate Fourier transforms when the order is higher than one. The equidistant nature of the Hermite interpolation basis functions allows for rapid Fourier transformations when the order is not very high, typically, smaller than four. And finally, the narrow support of the basis functions allows for a quick evaluation of functions.

A continuous spectral-path deformation was introduced into the spectral domain. Transformations to and from the complex spectral path were developed to allow for an efficient use of such a continuous spectral path. The main advantage of this continuous deformation is a significantly simpler formulation in the spectral domain, where the spectral domain is treated as a whole instead of being decomposed in distinct regions. A smaller number of simulation parameters is required with this continuous deformation, which allows for a simpler usage of the spatial spectral method.

An algorithm composed of a combination of the Hermite interpolation and a continuous spectral domain complex path was numerically tested against RCWA and FEM. A local relative difference smaller than 10^{-6} was observed against FEM in one case and $1.12 \cdot 10^{-3}$ against RCWA in the other. The convergence of the result against the key simulation parameters was shown for one example. A final example is shown where the algorithm is applied to a scattering problem of tens of wavelengths in size.

ACKNOWLEDGMENT

We are grateful to M. G. M. M. van Kraaij for generating reference data for the first testcase and to M. Pisarenco for providing reference data for the second testcase. This work is part of the research programme HTSM with project number 12786, which is (partly) financed by the Netherlands Organisation for Scientific Research (NWO).

REFERENCES

1. Dilz, R. J. and M. C. van Beurden, "An efficient complex spectral path formulation for simulating the 2D TE scattering problem in a layered medium using Gabor frames," *Journal of Computational Physics*, Vol. 345, 528–542, 2017.
2. Dilz, R. J., M. G. G. M. van Kraaij, and M. C. van Beurden, "2D TM scattering problem for finite objects in a dielectric stratified medium employing Gabor frames in a domain integral equation," *Journal of the Optical Society of America A*, Vol. 34, No. 8, 1315–1321, 2017.
3. Dilz, R. J., "A spatial spectral domain integral equation solver for electromagnetic scattering in dielectric layered media," PhD thesis, Chapter 8, Eindhoven University of Technology, 2017.
4. Dilz, R. J. and M. C. van Beurden, "Fast operations for a Gabor-frame based integral equation with equidistant sampling," *IEEE Antennas and Wireless Propagation Letters*, Vol. 12, No. 1, 82--85, 2018.
5. Zwamborn, P. and P. M. van den Berg, "The three-dimensional weak form of the conjugate gradient FFT method for solving scattering problems," *IEEE Trans. Microwave Theory Tech.*, Vol. 40, No. 9, 1757–1766, Sep. 1992.
6. Diebold, A. C., *Handbook of Silicon Semiconductor Metrology*, CRC Press, 2001.
7. Dilz, R. J. and M. C. van Beurden, "The Gabor frame as a discretization for the 2D transverse-electric scattering-problem domain integral equation," *Progress In Electromagnetics Research B*, Vol. 69, 117–136, 2016.
8. Chew, W. C., *Waves and Fields in Inhomogeneous Media*, IEEE Press, 1995.
9. Felsen, L. B. and N. Marcuvitz, *Radiation and Scattering of Waves*, IEEE Press, 1973.
10. Kong, J. A., *Theory of Electromagnetic Waves*, John Wiley & Sons, Inc, 1975.
11. Wait, J. R., *Electromagnetic Waves in Stratified Media*, Pergamon Press, 1970.
12. Sommerfeld, A., "Uber der ausbreitung der wellen in der drahtlosen telegraphie," *Annalen der Physik*, Vol. 333, No. 4, 665–736, 1909.
13. Hochman, A. and Y. Leviatan, "A numerical methodology for efficient evaluation of 2D Sommerfield integral in the dielectric half-space problem," *IEEE Transactions on Antennas and Propagation*, Vol. 58, No. 2, 413–431, Feb. 2010.
14. De Ruiter, H. M., "Limits on the propagation constants of planar optical waveguide modes," *Applied Optics*, Vol. 20, No. 5, 731–732, 1981.

15. Newman, E. H. and D. Forrai, "Scattering from a microstrip patch," *IEEE Transactions on Antennas and Propagation*, Vol. 35, No. 3, 245–251, Mar. 1987.
16. Larson, M. G. and F. Bengzon, *The Finite Element Method: Theory, Implementation, and Applications*, Springer, 2013.
17. Burger, S., L. Zschiedrich, J. Pomplun, and F. Schmidt, "Finite-element based electromagnetic field simulations: Benchmark results for isolated structures," *Proc. SPIE 8880 Photomask Technology*, Vol. 8880, 2013.
18. Moharam, M. G. and T. K. Gaylord, "Rigorous coupled-wave analysis of planar-grating diffraction," *Journal of the Optical Society of America*, Vol. 73, No. 4, 811–818, 1981.
19. Botten, I. C., M. S. Craig, R. C. McPhedran, J. L. Adams, and J. R. Andrewartha, "The dielectric lamellar diffraction grating," *Optica Acta*, Vol. 28, No. 3, 413–428, 1981.
20. Pisarenco, M., J. Maubach, I. Setija, and R. Mattheij, "Aperiodic Fourier modal method in contrast-field formulation for simulation of scattering from finite structures," *Journal of the Optical Society of America A*, Vol. 27, No. 11, 2423–2431, 2010.
21. Berezin, I. S. and N. P. Zhidkov, *Computing Methods*, Pergamon Press, 1965.
22. Dilz, R. J. and M. C. van Beurden, "Computational aspects of a spatial spectral domain integral-equation for scattering by objects of large longitudinal extent," *2017 International Conference on Electromagnetics in Advanced Applications (ICEAA)*, Verona, Italy, Sep. 11–15, 2017.
23. Taillaert, D., F. Van Laere, M. Ayre, W. Bogaerts, D. Van Thourhout, P. Bienstman, and R. Baets, "Grating couplers for coupling between optical fibers and nanophotonic waveguides," *Japanese Journal of Applied Physics*, Vol. 45, No. 8a, 6071–6077, 2006.
24. Lawrence, G. N., K. E. Moore, and P. J. Cronkite, "Rotationally symmetric construction optics for a waveguide focusing grating," *Appl. Opt.*, Vol. 29, No. 15, 2315–2319, May 1990.
25. Forouhar, S., R.-X. Lu, W. S. C. Chang, R. L. Davis, and S.-K. Yao, "Chirped grating lenses on nb2o5 transition waveguides," *Appl. Opt.*, Vol. 22, No. 19, 3128–3132, Oct. 1983.